



# Doped porous carbon nanostructures as non-precious metal catalysts prepared by amino acid glycine for oxygen reduction reaction

In-Ae Choi, Da-Hee Kwak, Sang-Beom Han, Jin-Young Park, Hyun-Seok Park, Kyeng-Bae Ma, Do-Hyoung Kim, Ji-Eun Won, Kyung-Won Park\*

Department of Chemical Engineering, Soongsil University, Seoul 156743, Republic of Korea

## ARTICLE INFO

### Article history:

Received 2 September 2016

Received in revised form 2 February 2017

Accepted 12 April 2017

Available online 20 April 2017

### Keywords:

Glycine

Doping source

Porous carbon

Non-precious metal catalyst

Oxygen reduction reaction

## ABSTRACT

To replace Pt-based catalysts for oxygen reduction reactions in polymer electrolyte membrane fuel cells, various carbon nanostructures doped by transition metals and heteroatoms have been investigated. In this study, we synthesized bi-modal porous iron and nitrogen doped carbon nanostructures as non-precious metal catalysts using glycine as a dopant and carbon source in the presence of iron salt. The samples exhibited a bi-modal porous structure consisting of macro- and meso-pores of 500 and 20 nm, respectively, and specific surface areas of 214–740 m<sup>2</sup> g<sup>−1</sup>, which facilitate electrochemical reactions due to increased amounts of electrochemical active sites and favorable mass transport. Furthermore, the porous carbon nanostructures showed considerable amounts of dopants, high crystallinity, and excellent electrical conductivity. Especially, the sample prepared using 500 and 20 nm silica beads with both glycine and iron salt showed improved catalytic activity in both acidic and alkaline media comparable to that of a commercial Pt catalyst.

© 2017 Elsevier B.V. All rights reserved.

## 1. Introduction

Polymer electrolyte membrane fuel cells (PEMFCs) are environment-friendly electrochemical energy sources that exhibit a relatively high power density, excellent energy conversion efficiency, and extremely low emission of pollutants [1,2]. However, since the oxygen reduction reaction (ORR) at the cathode in PEMFCs is sluggish, the loading amount of Pt-based catalysts at the cathode is higher than that of anode catalysts [3–5]. Thus, much effort has focused on developing advanced cathode catalysts, such as Pt-based alloys with second metal elements [6–8] or non-precious metal (NPM) structures [9,10]. Especially, transition metal chalcogenides [11,12], heteroatom-doped carbon materials [13,14], carbon nitride [15,16], and conducting polymers [17,18] have been reported to be promising candidate NPM catalysts for the ORR. Among these candidates, metal and nitrogen co-doped carbon based catalysts are attractive due to their low cost, enhanced durability, and ORR activity comparable to that of Pt catalysts [19,20].

In doped carbon structures, nitrogen as a dopant has a similar atomic size to carbon and 5 valence electrons, which results in formation of strong covalent bonds with surrounding carbon car-

bons. The doped nitrogen can donate free electrons in the carbon structure and plays a key role as an active site for ORR, resulting in improved ORR performance of nitrogen-doped carbons as cathode catalysts [21,22]. Nitrogen-doped carbon catalysts are synthesized using various nitrogen sources, such as urea, ammonia, and acetonitrile [23,24]. In 1964, cobalt phthalocyanine (Pc) as a NPM catalyst structure showed an electrocatalytic activity for ORR. The metal-N<sub>4</sub> macrocycles such as tetramethoxyphenylporphyrin (TMPP) and Pc, including transition metals such as Fe and Co, have been used as doping sources for the NPM catalysts under inert gas atmosphere at 400–1000 °C [25–30]. However, since metal-N<sub>4</sub>-macrocycles are expensive, toxic, and flammable, novel environment-friendly doping sources for the formation of metal-N<sub>4</sub>/C moieties have been suggested [31–37]. Especially, amino acids are relatively cheap, non-toxic, and contain various functional groups, such as –NH<sub>2</sub> and –COOH, and are thus favorable for the synthesis of nitrogen-doped carbon structures [37–39]. Among the amino acids, glycine (NH<sub>2</sub>CH<sub>2</sub>COOH) is abundant and has a relatively high atomic ratio of nitrogen to carbon, and so can be utilized as a nitrogen and carbon source for doped carbon structures as NPM catalysts [39–41]. Furthermore, the catalytic activity of the carbon-based NPM catalysts might be strongly dependent on pore structure and crystallinity. In particular, the bimodal porous structures having macropore and mesopore could increase catalytic active sites with specific surface areas and facilitate ion/charge transport [42]. The interconnected

\* Corresponding author.

E-mail address: [kwpark@ssu.ac.kr](mailto:kwpark@ssu.ac.kr) (K.-W. Park).

pore system of the 3D ordered bimodal structures could increase much electrical conductivity enhancing the ORR performance [43]. In this study, we synthesized co-doped porous carbon nanostructures as cathode catalysts using glycine as a nitrogen and carbon source with silica beads at 900 °C under an N<sub>2</sub> atmosphere. The samples were facilely prepared with pure 500 nm silica beads and a mixture of 500 and 20 nm silica beads in the absence and presence of FeCl<sub>2</sub>. The structure, morphology, and chemical states of the catalysts were characterized by scanning electron microscopy (SEM), transmission electron microscopy (TEM), X-ray diffraction (XRD), Raman spectroscopy, and X-ray photoelectron spectroscopy (XPS). The electrochemical properties of the samples as cathode catalysts in typical electrochemical cells were compared and evaluated using cyclic voltammetry and linear sweep voltammetry.

## 2. Experimental

### 2.1. Synthesis of doped porous carbon nanostructures

Glycine (0.4 g, Aldrich) was mixed and sonicated with pure 500 nm silica beads (Alfa Aesar) or a mixture of 500 and 20 nm beads (40% in water, Alfa Aesar) in the absence and presence of FeCl<sub>2</sub>·4H<sub>2</sub>O (0.044 g, Aldrich) in 50 ml de-ionized (DI) water. The weight ratios of glycine to 500 nm beads and 500 to 20 nm beads in the mixture were 1:1 and 3:1, respectively [44,45]. The completely dispersed solutions were poured into glass Petri dishes and dried in a 50 °C oven for 12 h (Fig. 1). The dried powder samples were heated in a tube furnace at 900 °C for 3 h under an N<sub>2</sub> atmosphere. The heated samples were stirred in 10 vol.% HF solution (J. T. Baker) for 2 h and then washed with DI water several times to remove silica beads and impurities. The washed samples were dried in a 50 °C oven for 24 h.

### 2.2. Structural analysis of doped porous carbon nanostructures

The morphology of the samples was observed using field emission scanning electron microscopy (FE-SEM, JEOL, JSM-7800F) at 5 kV. The structure and chemical composition of the samples were analyzed using field-emission transmission electron microscopy (FE-TEM, JEOL, JEM-ARM 200F) with a working voltage of 200 kV, and energy dispersive X-ray spectroscopy (EDX). XRD analysis was performed using a D2 phase system (BRUKER) with Cu K<sub>α</sub> radiation of  $\lambda = 1.54056 \text{ \AA}$  at 30 kV and 10 mA. Raman spectroscopy (Horiba Jobin Yvon, LabRAM HR UV/Vis/NIR PL) was carried out to confirm the crystallinity. The chemical states of the samples were observed using a XPS (Thermo scientific, K-Alpha) with an Al K<sub>α</sub> X-ray source of 1468.8 eV under a chamber pressure of  $7.8 \times 10^{-9}$  Torr. The surface area and pore structure were characterized using a nitrogen adsorption analyzer (Micromeritics ASAP 2020). The electrical conductivity of the pressed specimen was measured using the following equation:

$$\sigma = \frac{1}{\rho} = \frac{L}{RA} \quad (1)$$

where  $\sigma$  (S cm<sup>-1</sup>) is conductivity,  $\rho$  is resistivity,  $L$  is the thickness of the specimen,  $R$  is resistance, and  $A$  is the area of the specimen.

### 2.3. Electrochemical analysis of doped porous carbon nanostructures

The electrochemical properties of the samples were characterized in a typical electrochemical cell using a potentiostat (PGSTAT302N, AUTOLAB). The catalyst ink was prepared by mixing catalyst powder in de-ionized water, isopropanol, and 5 wt% Nafion solution (Aldrich). The ink was dropped on a rotating disk electrode (RDE) with an area of 0.070685 cm<sup>2</sup> and dried in a 50 °C oven for

10 min. After complete drying, the loading amount of the catalyst was 600  $\mu\text{g cm}^{-2}$ . The graphitic rod was used as a counter electrode. Ag/AgCl (in 3 M KCl) and Hg/HgO (in 1 M NaOH) were used as a reference electrode in acidic and alkaline solutions, respectively. Cyclic voltammograms (CVs) and linear sweep voltammograms (LSVs) of the samples were obtained in 0.5 M H<sub>2</sub>SO<sub>4</sub> and 0.1 M NaOH with a scan rate of 50 and 5 mV s<sup>-1</sup>, respectively. The oxygen polarization curves of the samples were measured using a rotating-ring disk electrode (RRDE, CH Instrument, CHI 700C). Graphitic rod and Ag/AgCl (in 3 M KCl) were used counter and reference electrodes, respectively. The areas of the working and Pt-ring electrodes were 0.1257 and 0.1885 cm<sup>2</sup>, respectively. The catalyst ink was prepared by mixing catalyst powder in de-ionized water, isopropanol, and 5 wt% Nafion solution (Aldrich). The ink was dropped on a RRDE and dried in a 50 °C oven for 10 min. After complete drying, the loading amount of the catalyst was 600  $\mu\text{g cm}^{-2}$ . In the ORR measurement, the Pt-ring electrode was applied at 1.15 V. Stability testing of the samples for the ORR was conducted by scanning for 10,000 cycles in O<sub>2</sub>-saturated solutions with a scan rate of 50 mV s<sup>-1</sup>. All electrode potentials were converted to reversible hydrogen electrode (RHE).

## 3. Results and discussion

Fig. 2(a)–(h) show FE-SEM and TEM images of the samples synthesized using glycine as a nitrogen and carbon source with pure 500 nm silica beads and a mixture of 500 and 20 nm silica beads. The samples synthesized using the pure 500 nm silica template exhibited a well-stacked porous structure with macro-pores of 500 nm in the absence (Fig. 2(a) and (e)) and presence (Fig. 2(c) and (g)) of FeCl<sub>2</sub> (denoted as G-500 and FeG-500, respectively). However, the samples synthesized using the mixture of 500 and 20 nm silica beads showed a bimodal porous structure with macro-pores of 500 nm surrounded by 20 nm meso-pores in the absence (Fig. 2(b) and (f)) and presence (Fig. 2(d) and (h)) of FeCl<sub>2</sub> (denoted as G-500/20 and FeG-500/20, respectively). This implies that the samples with well-defined pore structures could be formed by the replica method using silica beads. As shown in high-resolution TEM images of G-500, G-500/20, FeG-500, and FeG-500/20 in Fig. 2(i)–(l), the samples displayed d-spacings of 0.34–0.37 nm. Especially, the FeG-500 and FeG-500/20 exhibited an improved crystal structure with d-spacings of 0.342 and 0.34 nm, respectively (Fig. 2(k) and (l), respectively) [46,47]. Furthermore, to confirm the elemental distribution of the samples, STEM-EDX elemental mapping analysis was carried out as indicated in Fig. 2(m)–(p). All samples revealed a homogeneous nitrogen distribution in the carbon matrix, formed by glycine as nitrogen and carbon source, and G-500, G-500/20, FeG-500, and FeG-500/20 contained 2.96, 4.56, 0.96, and 5.24 at% of N, respectively. The FeG-500 and FeG-500/20 included 0.04 and 0.06 at% Fe, respectively, as well as N, due to use of iron salt during the synthesis.

To further characterize the crystal structure of the catalysts, XRD patterns and Raman spectra were obtained (Fig. 3). In the XRD data of Fig. 3(a), all samples exhibited (002) and (101) peaks at  $2\theta = 26^\circ$  and  $42^\circ$ , respectively, which are associated with the crystal structure of graphitic carbon. In particular, it is remarkable that FeG-500 and FeG-500/20 had diffraction patterns distinct from those of G-500 and G-500/20, demonstrating enhanced crystallinity of the carbon structure synthesized in the presence of FeCl<sub>2</sub> [48–50]. As shown in Fig. 3(b), the Raman spectra contained peaks at 1368 and 1590 cm<sup>-1</sup>, corresponding to D- and G-bands, respectively, which are associated with the vibration modes of sp<sup>3</sup> in disordered graphene and graphitic sp<sup>2</sup> carbon, respectively [40,51]. FeG-500 and FeG-500/20 contained more distinct characteristic peaks, compared to the G-500 and G-500/20, and 2D-band located at 2690 cm<sup>-1</sup> [52,53]. Thus, from the XRD and Raman analysis, it can

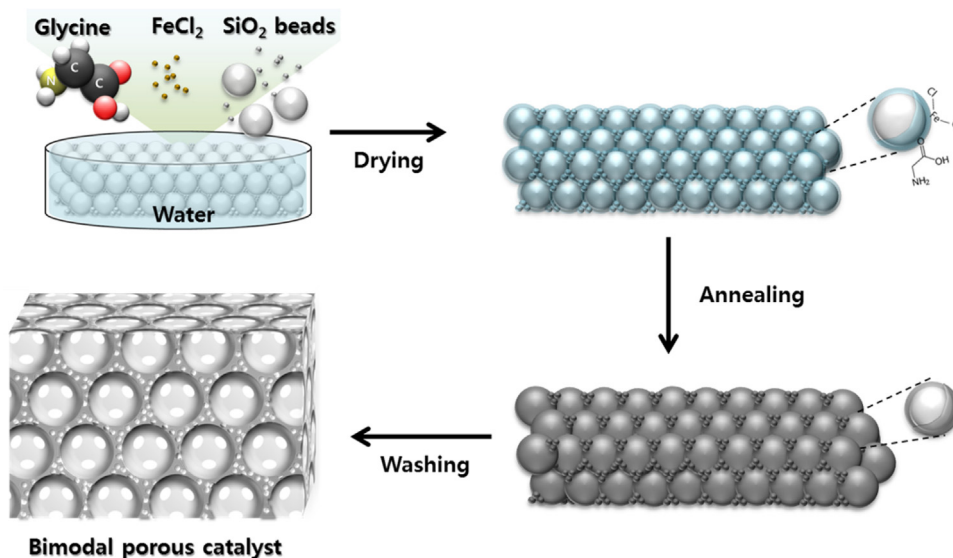


Fig. 1. Scheme illustration of synthesis procedure of doped porous carbon nanostructures.

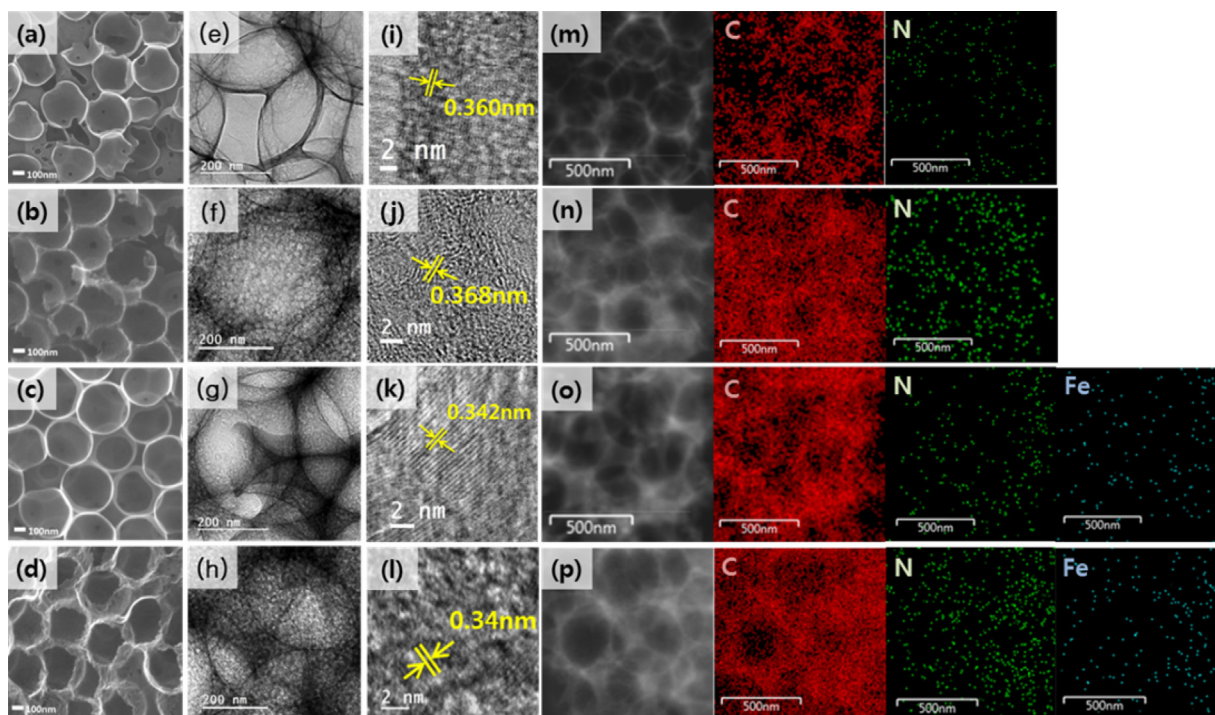


Fig. 2. FE-SEM, FE-TEM, HR-TEM, and STEM-EDX elemental mapping images of (a, e, i, m) G-500, (b, f, j, n) G-500/20, (c, g, k, o) FeG-500, and (d, h, l, p) FeG-500/20.

be concluded that the samples synthesized in the presence of FeCl<sub>2</sub> had a higher crystallinity than those synthesized without FeCl<sub>2</sub>.

Fig. 4 shows the nitrogen adsorption–desorption isotherms and pore size distributions of the catalysts. Compared to the G-500 and FeG-500 samples, which were synthesized with pure 500 nm beads, G-500/20 and FeG-500/20, which were prepared using a mixture of 500 and 20 nm beads, exhibited a typical IV-type isotherm curve with meso-pores of 20 nm. The formation of 20 nm meso-pores in G-500/20 and FeG-500/20 suggests that the well-defined porous structure was completely transferred by the replica method using silica beads. The specific active surface areas of G-500, G-500/20, FeG-500, and FeG-500/20 were 214, 324, 455, and 740 m<sup>2</sup> g<sup>−1</sup>, respectively. In particular, the surface area of G-500/20 and FeG-500/20 was 1.5 and 1.6 times higher than that of G-500 and

FeG-500, respectively, which suggested improvement factor by the addition of 20 nm sized silica bead in the template. However, it is noticeable that FeG-500/20 had the largest specific surface area due to its well-formed porous graphitic carbon nanostructure resulting from the heating process using mixed beads in the presence of FeCl<sub>2</sub> [54].

The electrical conductivity of the catalysts was determined (Fig. 5). The samples synthesized using glycine as a carbon and nitrogen source exhibited a conductivity of 8.2–21.4 S cm<sup>−1</sup>, which was higher than that of carbon black (~1.36 S cm<sup>−1</sup>). The high conductivity of FeG-500 and FeG-500/20 is attributed to enhanced crystallinity of the carbon structure formed with iron salt, as reported previously using HR-TEM, XRD, and Raman analysis, in comparison with G-500 and G-500/20 [2]. It is also interesting

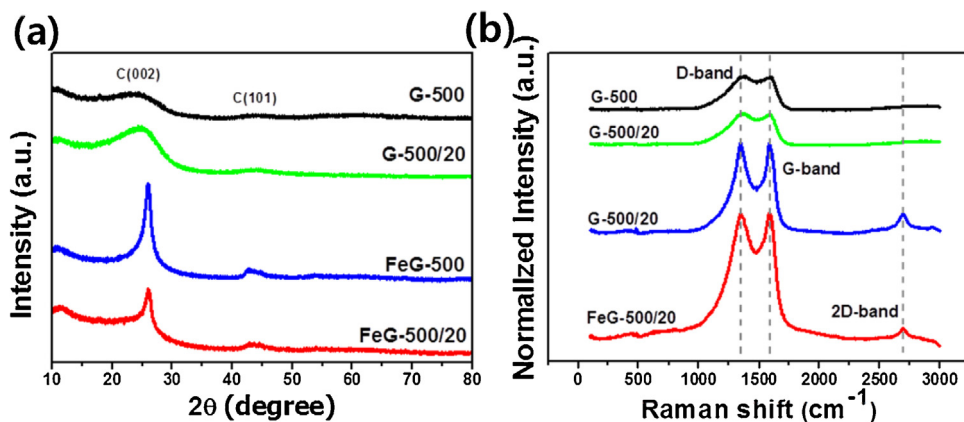


Fig. 3. (a) Wide-angle XRD patterns and (b) Raman spectra of G-500, G-500/20, FeG-500, and FeG-500/20.

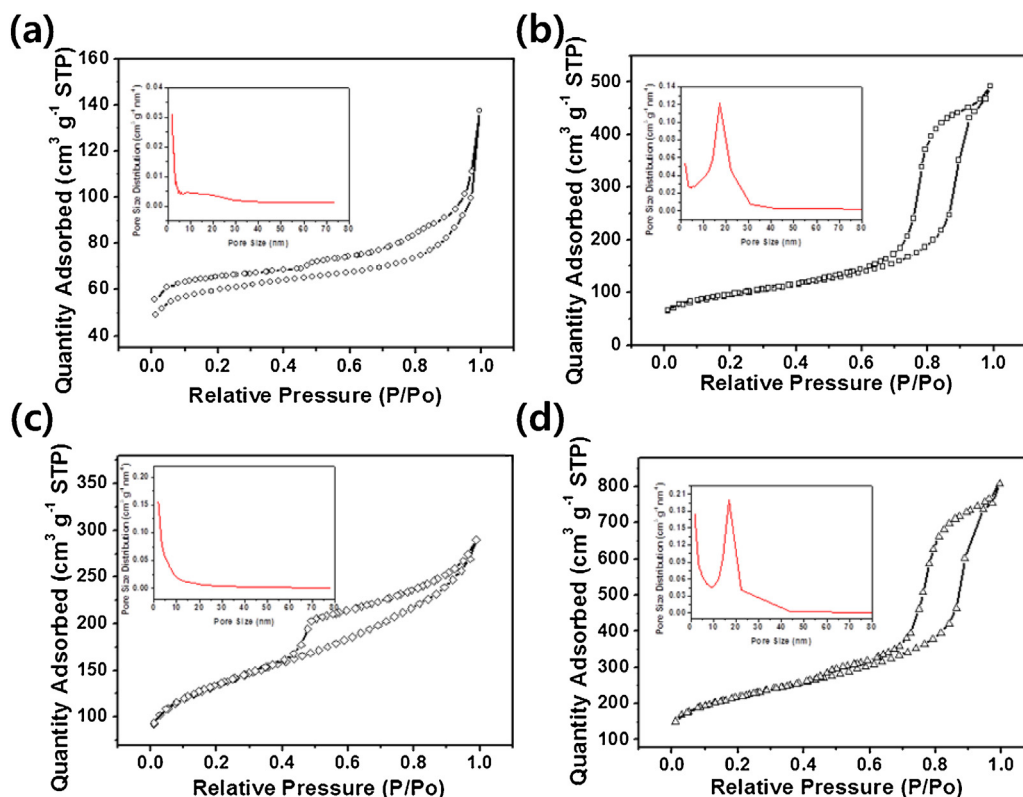


Fig. 4. N<sub>2</sub> adsorption-desorption isotherms and pore size distributions (insets) of (a) G-500, (b) G-500/20, (c) FeG-500, and (d) FeG-500/20.

that G-500/20 and FeG-500/20, which had a bimodal porous structure, showed improved conductivity due to a highly dense stacking electrode structure with the gaps between which are filled with meso-sized particles favorable for electron conduction, compared to G-500 and FeG-500, which had a single pore size [43,55].

To accurately investigate the composition and chemical state of the samples, XPS spectra were obtained (Fig. 6). Although the distribution amount of the elements in the sample were observed by EDX (Fig. 2), XPS analysis under a high vacuum can provide more accurate quantity of the elements on the surface of the samples. The amount of nitrogen as a dopant in G-500, G-500/20, FeG-500, and FeG-500/20 was 5.57, 5.85, 3.21, and 4.37 at%, respectively. FeG-500 and FeG-500/20 contained 0.12 and 0.16 at% Fe as a dopant, respectively. The N 1s spectra of the samples consisted of pyridinic, pyrrolic, graphitic, and oxidized N states located at binding energies of 398.25–398.7, 399.78–400.05, 400.99–401.16,

and 402–404.27 eV, respectively (Fig. 6(a)–(d)). Graphitic N predominated in all samples. G-500 and G-500/20 exhibited similar proportions of pyridinic and pyrrolic states. However, it is interesting that the pyridinic N states in FeG-500 and FeG-500/20 were increased due to the formation of a well-doped carbon nanostructure in the presence of iron compared to G-500 and G-500/20 (Fig. 6(e)) [56,57]. Nitrogen-doped carbon catalysts with a dominant pyridinic N state have improved electrocatalytic activity toward ORR [24,58,59]. The pyridinic N state could induce formation of unshared electron pairs in the carbon edges and so enhance improved electron sharing [60]. The carbon-neighboring pyridinic N state might show Lewis basicity and improve oxygen adsorption, thus enhancing ORR activity [61]. As shown in Fig. 6(f) and (g), FeG-500 and FeG-500/20 contained the Fe 2p spectra of Fe(II) and Fe(III), which enhance their crystal structure, electrical conductivity, and specific surface area [61]. Furthermore, the iron states conjugated

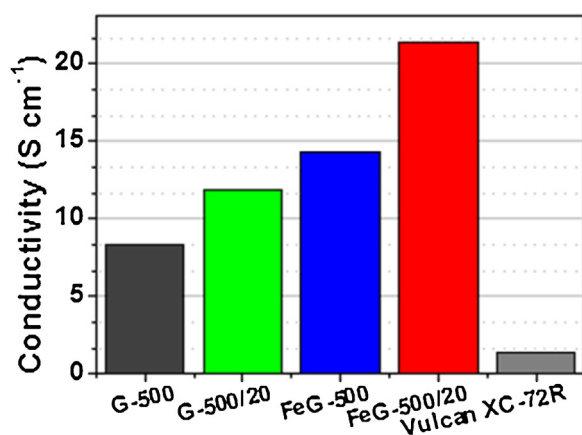


Fig. 5. Electrical conductivity of G-500, G-500/20, FeG-500, FeG-500/20, and Vulcan XC-72R.

with nitrogen in the doped carbon structures might function as active sites for ORR [56,62–65].

Fig. 7(a)–(d) show the CVs of the doped carbon nanostructures as cathode catalysts for PEMFC in Ar- and O<sub>2</sub>-saturated 0.5 M H<sub>2</sub>SO<sub>4</sub> with a scan rate of 50 mV s<sup>−1</sup> at 25 °C. The characteristic peaks of the ORR in all samples appeared in O<sub>2</sub>-saturated 0.5 M H<sub>2</sub>SO<sub>4</sub>. The ORR peak potentials of G-500, G-500/20, FeG-500, and FeG-500/20 were 0.30, 0.41, 0.66, and 0.71 V vs. RHE, respectively. Since a high peak potential implies that the sample has improved ORR properties, FeG-500/20 can be expected to exhibit the highest ORR activity. Furthermore, the characteristic peaks for all samples in Ar-saturated 0.5 M H<sub>2</sub>SO<sub>4</sub> were compared (Fig. 7(e)). The specific capacitances of G-500, G-500/20, FeG-500, and FeG-500/20 were determined to be 23.8, 51.5, 74.5, and 121.0 F g<sup>−1</sup>, respectively (Fig. 7(f)) by the following equation:

$$C_{cv}(v) = \frac{1}{2m\Delta V} [Q_d(v) + Q_c(v)] \quad (2)$$

In general, the high capacitance of carbon-based electrodes in the ionic solutions reflects improved electrochemical active sites, which facilitates mass transport due to the porous structure and increased surface area of the electrodes [20,55,66–69]. Among the samples, FeG-500/20 exhibited the highest ORR peak potential and specific capacitance due to its bimodal porous carbon nanostructure and co-doping by N and Fe.

To further characterize and compare ORR activity, the LSVs of the doped carbon nanostructures were obtained in O<sub>2</sub>-saturated 0.5 M H<sub>2</sub>SO<sub>4</sub> at different rotating speeds as shown in Fig. 8(a)–(d). In the ORR curves of the samples at 1600 rpm, FeG-500 and FeG-500/20 exhibited considerable oxygen reduction activities with activation, ohmic, and diffusion polarizations (Fig. 8(e)). The ORR current densities at 0.8 V and half-wave potentials of G-500, G-500/20, FeG-500, and FeG-500/20 were 0.06, 0.13, 0.20, and 2.15 mA cm<sup>−2</sup>, and 0.38, 0.46, 0.62, and 0.79 V vs. RHE, respectively. Although the amounts of nitrogen states, which function as ORR active sites, in G-500 and G-500/20 were higher than those in FeG-500 and FeG-500/20, FeG-500 and FeG-500/20, which have higher ratios of pyridinic N, showed enhanced ORR activity. The bimodal porous structure of FeG-500/20 could facilitate mass transport of oxygen and by-products during the ORR process. The relatively high specific surface area and dominant pyridinic N state of FeG-500/20 might provide an increased amount of electrochemical active sites for ORR. As a result, the enhanced ORR activity of FeG-500/20 can be attributed to a synergistic effect of its bimodal porous structure, high specific surface area, co-doping, and dominant pyridinic nitrogen state.

The ORR performance of the samples was evaluated using an RRDE measurement, as shown in Fig. 9. The RRDE polarization curves of the samples were obtained in O<sub>2</sub>-saturated 0.5 M H<sub>2</sub>SO<sub>4</sub> with a scan rate of 5 mV s<sup>−1</sup> and an electrode rotation rate of 1600 rpm at 25 °C (Fig. 9(a)). In the RRDE curves, the disk current density (*I<sub>D</sub>*) is associated with the main reaction in the ORR (O<sub>2</sub> + nH<sup>+</sup> + ne<sup>−</sup> → xH<sub>2</sub>O + yH<sub>2</sub>O<sub>2</sub>) and the ring current density (*I<sub>R</sub>*) is related to the oxidation reaction of peroxide (H<sub>2</sub>O<sub>2</sub> → O<sub>2</sub> + 2H<sup>+</sup> + 2e<sup>−</sup>), which is a by-product of ORR. The order of *I<sub>D</sub>* for the samples was G-500 < G-500/20 < FeG-500 < FeG-500/20, which was in agreement with the LSV result. As shown in Fig. 9(b), the electron-transfer number (*n*) and %H<sub>2</sub>O<sub>2</sub> of the samples for ORR could be determined using the following equations:

$$n = \frac{4I_D}{I_D + I_R/N} \quad (3)$$

$$\%H_2O_2 = \frac{200I_R}{I_D N + I_R} \quad (4)$$

where *I<sub>D</sub>*, *I<sub>R</sub>*, and *N* are the current on the carbon disk, the current on the Pt-ring electrode, and the collecting coefficient number (−0.4245 in this case), respectively. In particular, FeG-500/20 exhibited a four-electron reaction and low concentration of H<sub>2</sub>O<sub>2</sub>

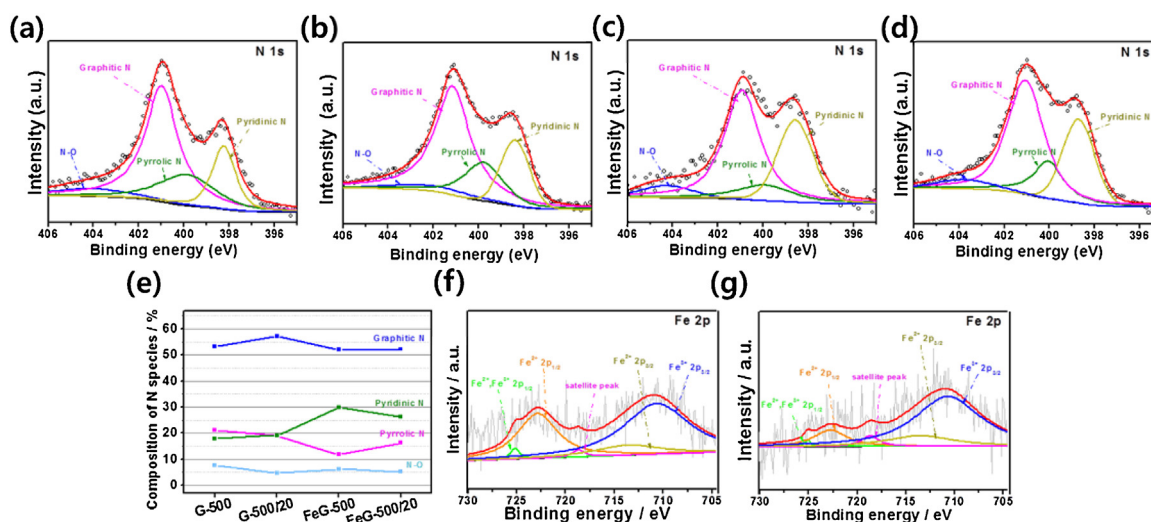
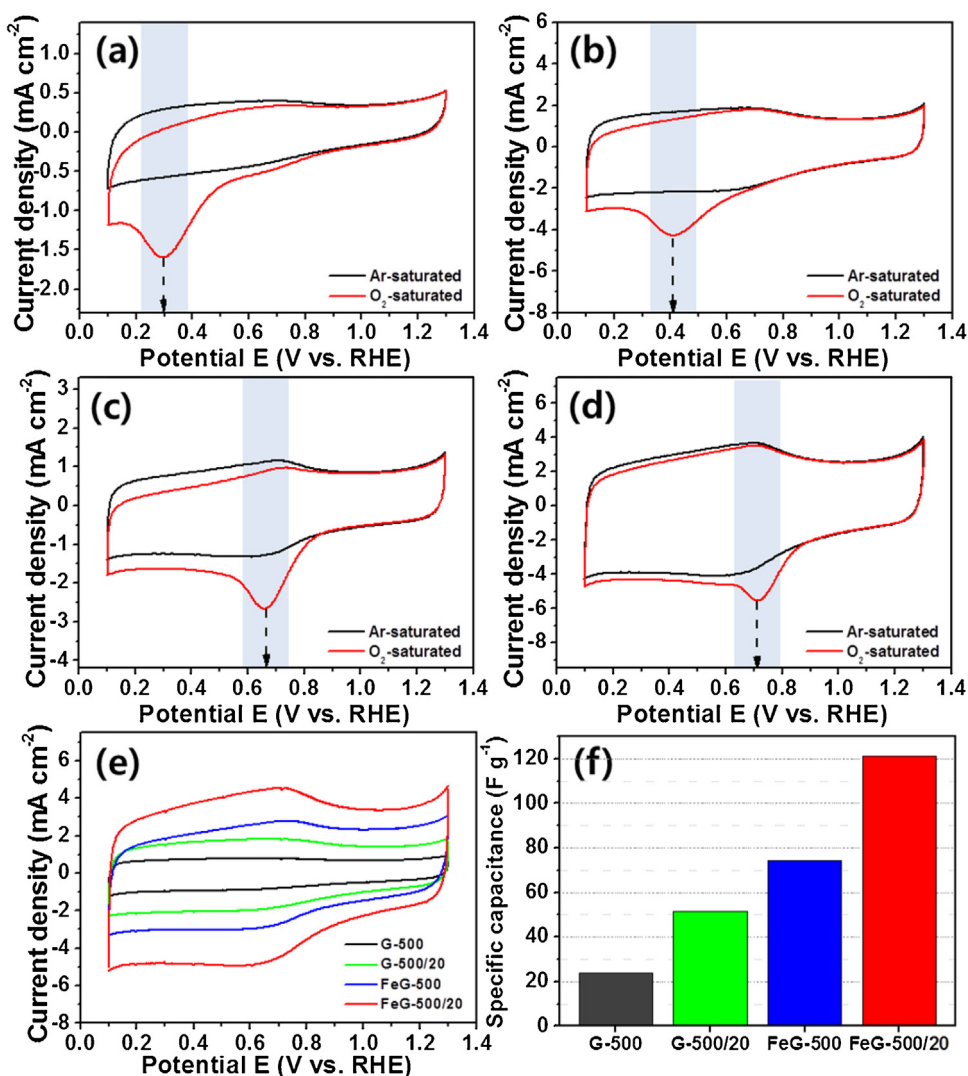


Fig. 6. N 1s XPS spectra of (a) G-500, (b) G-500/20, (c) FeG-500, and (d) FeG-500/20. (e) Comparison of nitrogen species of the samples. Fe 2p XPS spectra of (f) FeG-500 and (g) FeG-500/20.



**Fig. 7.** CVs of (a) G-500, (b) G-500/20, (c) FeG-500, and (d) FeG-500/20 in Ar- and O<sub>2</sub>-saturated 0.5 M H<sub>2</sub>SO<sub>4</sub> in with a scan rate of 50 mV s<sup>-1</sup> at 25 °C. Comparison of (e) CVs and (f) specific capacitances of the samples in Ar-saturated 0.5 M H<sub>2</sub>SO<sub>4</sub> with a scan rate of 50 mV s<sup>-1</sup> at 25 °C.

in the applied potential range, demonstrating a complete ORR process comparable to a commercial Pt/C catalyst (denoted as comm. Pt/C); i.e., improved activity of FeG-500/20 in an acidic medium.

Furthermore, to evaluate ORR activity in an alkaline medium, the LSVs of FeG-500/20 and comm. Pt/C as cathode catalysts were obtained in O<sub>2</sub>-saturated 0.1 M NaOH at a rotating speed of 1600 rpm, as shown in Fig. 10(a). The specific current densities at 0.9 V and half-wave potentials of FeG-500/20 and comm. Pt/C were 1.42 and 0.70 mA cm<sup>-2</sup> and 0.87 and 0.85 V, respectively, demonstrating better electrocatalytic activity of FeG-500/20 toward ORR in alkaline solution compared to comm. Pt/C. FeG-500/20 exhibited considerably improved ORR activity in an alkaline solution compared to acidic solution, due to the lower overpotential for ORR in O<sub>2</sub>-saturated alkaline medium compared to that in acidic medium [70]. To evaluate the ORR stability of the catalysts, ORR polarization curves of FeG-500/20 and comm. Pt/C before and after 10,000 potential cycling (accelerated stability test, AST) were recorded (Fig. 10(c) and (d)). The AST was carried out between 0.7 and 1.2 V (50 mV s<sup>-1</sup>) with a rotation speed of 1600 rpm in O<sub>2</sub>-saturated 0.1 M NaOH. FeG-500/20 and comm. Pt/C exhibited different half-wave potentials ( $\Delta E_{1/2}$ ) before and after stability testing of ~4.6 and ~26.1 mV, respectively. This demonstrates that FeG-500/20 has improved stability for the ORR in alkaline medium

compared to comm. Pt/C. To identify the effect of iron as an electrocatalytic active site, the LSVs of FeG-500/20 were determined in O<sub>2</sub>-saturated 0.1 M NaOH in the absence and presence of 10 mM KCN (Fig. 11). CN<sup>-</sup> ions can selectively adsorb transition metal elements, such as Fe [71–73]. Since the CN<sup>-</sup> adsorption on Fe sites in FeG-500/20 reduces the number of active sites available for ORR, FeG-500/20 exhibited dramatically deteriorated ORR activity; i.e., a reduction in half-wave potential of ~74 mV in O<sub>2</sub>-saturated 0.1 M NaOH in the presence of KCN. Table 1 shows comparison of state-of-the-art NPM cathode catalysts. The NPM catalysts with doped nanostructures have been mainly synthesized using TMPP, biomaterials, and biomass as precursors and dopants. Compared to the NPM catalysts, FeG-500/20 synthesized using 500 and 20 nm silica beads with glycine and iron salt showed enhanced ORR activity in both acid and alkaline media. The enhanced ORR performance of FeG-500/20 was attributed to the excellent crystal structure and electrical conductivity, increased nitrogen and iron co-doping sites with a large specific surface area, and a bimodal porous structure consisting of macro- and meso-pores. Thus, FeG-500/20, which has a bimodal porous structure and was synthesized using glycine, can likely be utilized as a cathode catalyst for PEMFCs.

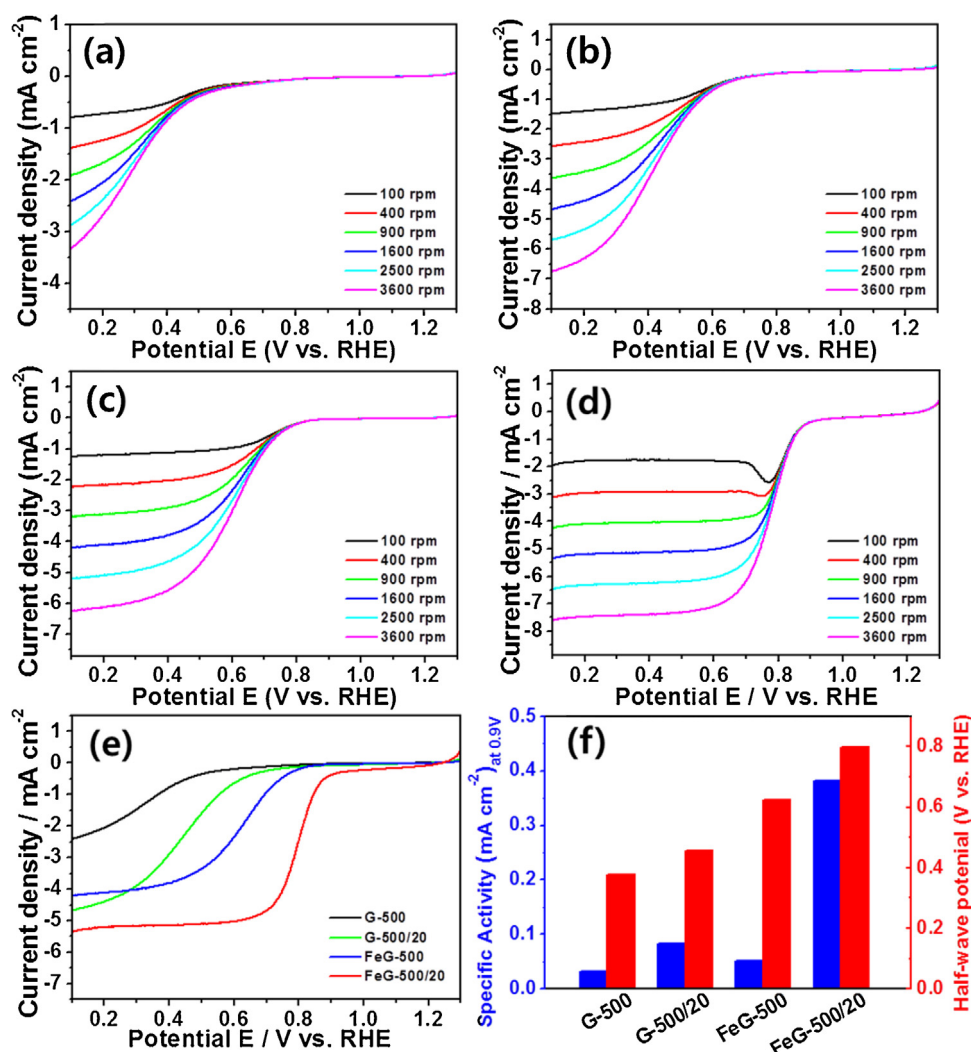


**Fig. 8.** LSVs (a) G-500, (b) G-500/20, (c) FeG-500 and (d) FeG-500/20 in O<sub>2</sub>-saturated 0.5 M H<sub>2</sub>SO<sub>4</sub> with a scan rate of 5 mV s<sup>-1</sup>. (e) LSVs of the samples with a scan rate of 5 mV s<sup>-1</sup> and an electrode rotation rate of 1600 rpm in O<sub>2</sub>-saturated 0.5 M H<sub>2</sub>SO<sub>4</sub>. (f) Comparison of the specific activities at 0.9 V and half-wave potentials for the samples.

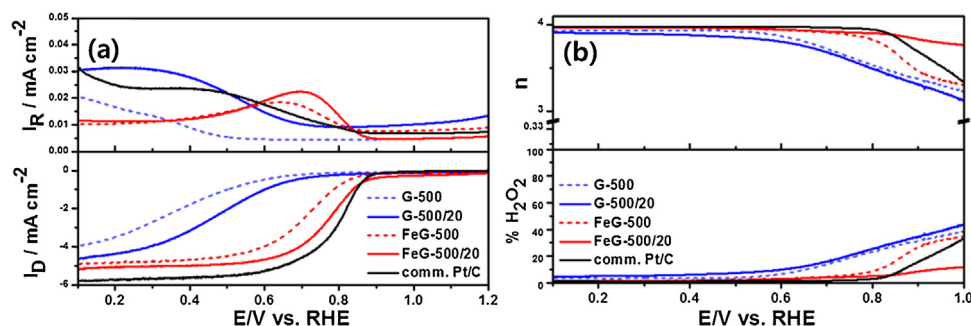


**Fig. 9.** (a) RRDE polarization curves of the samples in O<sub>2</sub>-saturated 0.5 M H<sub>2</sub>SO<sub>4</sub> with a scan rate of 5 mV s<sup>-1</sup> and an electrode rotation rate of 1600 rpm at room temperature. (b) Electron-transfer number and %H<sub>2</sub>O<sub>2</sub> of the samples for ORR.

#### 4. Conclusions

In summary, we synthesized an iron- and nitrogen-doped porous carbon nanostructure as a cathode catalyst using FeCl<sub>2</sub>·4H<sub>2</sub>O as a metal source and glycine as a nitrogen and carbon source with 500 and 20 nm silica beads as templates. The samples exhibited a well-stacked porous structure, homogeneous doping, relatively high specific surface area, and improved crystallinity. Especially, FeG-500/20 showed a high half-wave potential,

improved specific activity, and complete ORR comparable to commercial Pt/C catalyst. The enhanced ORR properties of FeG-500/20 are attributed to its porous nanostructure with a high specific surface area, improved crystallinity for electrical conduction, the generation of active site due to the Fe doping, and high ratio of a pyridinic N state. The doped porous carbon nanostructure prepared using glycine with silica beads can thus likely be utilized as an NPM catalyst for the ORR in both acidic and alkaline media.

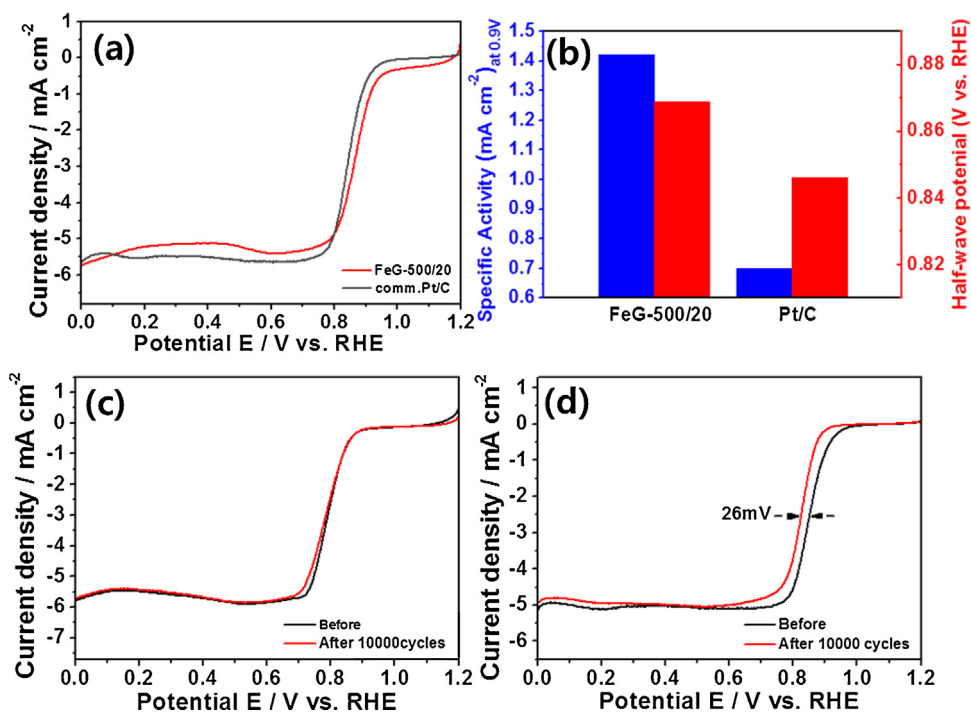


**Fig. 10.** (a) LSVs of FeG-500/20 and commercial Pt/C with a scan rate of 5 mV s<sup>-1</sup> and an electrode rotation rate of 1600 rpm in O<sub>2</sub>-saturated 0.1 M NaOH. (b) Comparison of the specific activities at 0.9 V and half-wave potentials for the samples. ORR polarization curves of (c) FeG-500/20 and (d) comm. Pt/C before and after stability testing in O<sub>2</sub>-saturated 0.1 M NaOH solution with a scan rate of 5 mV s<sup>-1</sup> and an electrode rotation speed of 1600 rpm.

**Table 1**

Comparison of state-of-the-art NPM cathode catalysts for the PEMFC.

Catalysts	Precursor	Metal	Electrolyte	BET surface area (m <sup>2</sup> g <sup>-1</sup> )	Surface nitrogen content (at.%)	Surface other atom content (at.%)	$\Delta E_{1/2}^a$ (mV)	Ref
FeG-500/20	<b>Glycine</b>	<b>FeCl<sub>2</sub></b>	<b>0.5 M H<sub>2</sub>SO<sub>4</sub></b>	<b>740</b>	<b>4.37</b>	<b>0.16 (Fe)</b>	<b>-10.1</b>	This study
FeCo-OMPC	FeTMPP CoTMPP	0.1 M HClO <sub>4</sub>	1190	5.4	4.8(2.5 Fe, 2.3 Co)	5.0	[25]	
Fe <sub>3</sub> C/NG-800	1,8-Diaminonaphthalene	FeCl <sub>3</sub>	0.1 M HClO <sub>4</sub>	920.6	3.78	0.81 (Fe)	-71	[19]
NCS-800	Plant Typha orientalis	-	0.5 M H <sub>2</sub> SO <sub>4</sub>	646	9.1	-	-110	[33]
N-CNF aerogel	Bacterial cellulose	-	0.5 M H <sub>2</sub> SO <sub>4</sub>	916	5.8	-	-190	[74]
PAA-CYS	Cysteine (amino acid)	FeCl <sub>2</sub>	0.1 M HClO <sub>4</sub>	180.5	1.3	0.4 (S)	-300	[39]
PAA-GLY	Glycine	FeCl <sub>2</sub>	0.1 M HClO <sub>4</sub>	150.6	2.3	-	-450	[39]
Fe/N/CNT@PCF	Catkin (from Plant)	FeCl <sub>3</sub>	0.5 M H <sub>2</sub> SO <sub>4</sub>	461.5	4.15	1.7 (Fe)	-480	[63]
FeG-500/20	<b>Glycine</b>	<b>FeCl<sub>2</sub></b>	<b>0.1 M NaOH</b>	<b>740</b>	<b>4.37</b>	<b>0.16 (Fe)</b>	<b>22.8</b>	This study
Fe-PANI-C/Mela	Aniline, Melamine	FeCl <sub>3</sub>	0.1 M KOH	702	1.9	0.68 (Fe)	20.0	[75]
Fe <sub>3</sub> C/NG-800	1,8-Diaminonaphthalene	FeCl <sub>3</sub>	0.1 M KOH	920.6	3.78	0.81	24	[19]
HNORI-M-AT	Nori, Melamine	-	0.1 M KOH	538	2.63	(0.23, S)	11	[76]
NCS-800	Plant Typha orientalis	-	0.1 M KOH	646	9.1	-	5	[33]
Chitin-900	Prawn	-	0.1 M KOH	526	5.9	-	5	[77]
HMCS-1	Glycine	-	0.1 M KOH	451	3.82	-	0.1	[40]
Mn-CN <sub>x</sub>	Glycine	KMnO <sub>4</sub>	0.1 M KOH	-	4.8	-	-12	[41]
HC-900	Human Hair	-	0.1 M KOH	1813.95	3.80	1.73 (S)	-20	[34]
Fe/N/CNT@PCF	Catkin (from Plant)	FeCl <sub>3</sub>	0.1 M KOH	461.5	4.15	1.7 (Fe)	-23	[63]
N-CNF aerogel	Bacterial cellulose	-	0.1 M KOH	916	5.8	-	-50	[74]
Fe/C-SOYB-A	Soybean	FeCl <sub>3</sub>	0.1 M KOH	-	-	-	-170	[36]

<sup>a</sup> Difference between half wave potential of prepared catalysts and commercial Pt/C catalyst ( $\Delta E_{1/2} = E_{1/2}(\text{prepared catalysts}) - E_{1/2}(\text{comm. Pt/C})$ ).

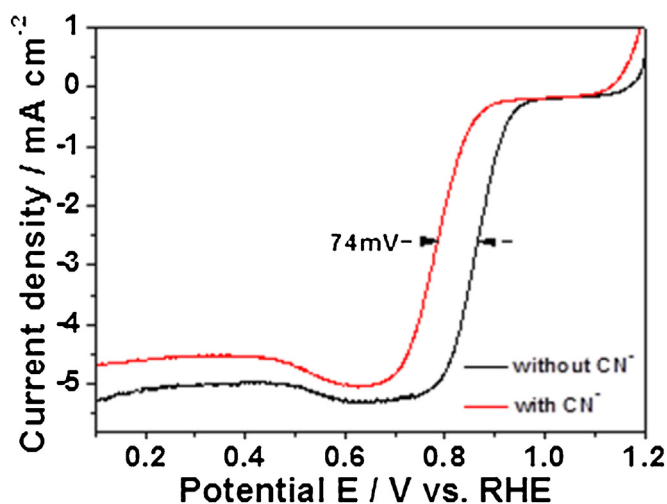


Fig. 11. Polarization curves of FeG-500/20 with a scan rate of  $5 \text{ mV s}^{-1}$  and an electrode rotation speed of 1600 rpm in  $\text{O}_2$ -saturated  $0.1 \text{ M NaOH}$  in the absence and presence of  $10 \text{ mM KCN}$ .

### Conflicts of interest

The authors declare no competing financial interest.

### Acknowledgment

This research was supported by Basic Science Research Program through the National Research Foundation of Korea (NRF) funded by the Ministry of Education (NRF-2016R1A2B2016033).

### References

- [1] G. Wu, P. Zelenay, Nanostructured nonprecious metal catalysts for oxygen reduction reaction, *Acc. Chem. Res.* 46 (2013) 1878–1889.
- [2] D.-S. Yang, M.Y. Song, K.P. Singh, J.-S. Yu, The role of iron in the preparation and oxygen reduction reaction activity of nitrogen-doped carbon, *Chem. Commun.* 51 (2015) 2450–2453.
- [3] H. Liang, W. Wei, Z.-S. Wu, X. Feng, K. Müllen, Mesoporous metal–nitrogen-doped carbon electrocatalysts for highly efficient oxygen reduction reaction, *J. Am. Chem. Soc.* 135 (2013) 16002–16005.
- [4] L. Yang, Y. Su, W. Li, X. Kan, Fe/N/C electrocatalysts for oxygen reduction reaction in PEM fuel cells using nitrogen-rich ligand as precursor, *J. Phys. Chem. C* 119 (2015) 11311–11319.
- [5] Y. Shao, J. Sui, G. Yin, Y. Gao, Nitrogen-doped carbon nanostructures and their composites as catalytic materials for proton exchange membrane fuel cell, *Appl. Catal. B: Environ.* 79 (2008) 89–99.
- [6] J. Zhang, H. Yang, J. Fang, S. Zou, Synthesis and oxygen reduction activity of shape-controlled  $\text{Pt}_3\text{Ni}$  nanopolyhedra, *Nano Lett.* 10 (2010) 638–644.
- [7] X. Wang, M. Vara, M. Luo, H. Huang, A. Ruditskiy, J. Park, S. Bao, J. Liu, J. Howe, M. Chi, Z. Xie, Y. Xia, Pd@Pt core-shell concave decahedra: a class of catalysts for the oxygen reduction reaction with enhanced activity and durability, *J. Am. Chem. Soc.* 137 (2015) 15036–15042.
- [8] Y. Bing, H. Liu, L. Zhang, D. Ghosh, J. Zhang, Nanostructured Pt-alloy electrocatalysts for PEM fuel cell oxygen reduction reaction, *Chem. Soc. Rev.* 39 (2010) 2184–2202.
- [9] G. Wu, K.L. More, C.M. Johnston, P. Zelenay, High-performance electrocatalysts for oxygen reduction derived from polyaniline, iron, and cobalt, *Science* 332 (2011) 443–447.
- [10] X. Li, B.N. Popov, T. Kawahara, H. Yanagi, Non-precious metal catalysts synthesized from precursors of carbon, nitrogen, and transition metal for oxygen reduction in alkaline fuel cells, *J. Power Sources* 196 (2011) 1717–1722.
- [11] B. Yu, W. Wu, J. Jin, H. Wu, S. Wang, Q. Xia, Facile synthesis of Co-based selenides for oxygen reduction reaction in acidic medium, *Int. J. Hydrogen Energy* 41 (2016) 8863–8870.
- [12] Y. Feng, T. He, N. Alonso-Vante, In situ free-surfactant synthesis and ORR-electrochemistry of carbon-supported  $\text{Co}_3\text{S}_4$  and  $\text{CoSe}_2$  nanoparticles, *Chem. Mater.* 20 (2008) 26–28.
- [13] Z. Yang, Z. Yao, G. Li, G. Fang, H. Nie, Z. Liu, X. Zhou, X. Chen, S. Huang, Sulfur-doped graphene as an efficient metal-free cathode catalyst for oxygen reduction, *ACS Nano* 6 (2012) 205–211.
- [14] J. Zhang, Z. Zhao, Z. Xia, L. Dai, A metal-free bifunctional electrocatalyst for oxygen reduction and oxygen evolution reactions, *Nat. Nanotechnol.* 10 (2015) 444–452.
- [15] X. Wang, L. Wang, F. Zhao, C. Hu, Y. Zhao, Z. Zhang, S. Chen, G. Shi, L. Qu, Monoatomic-thick graphitic carbon nitride dots on graphene sheets as an efficient catalyst in the oxygen reduction reaction, *Nanoscale* 7 (2015) 3035–3042.
- [16] J. Liang, Y. Zheng, J. Chen, J. Liu, D. Hulicova-Jurcakova, M. Jaroniec, S.Z. Qiao, Facile oxygen reduction on a three-dimensionally ordered macroporous graphitic  $\text{C}_3\text{N}_4$ /carbon composite electrocatalyst, *Angew. Chem. Int. Ed.* 124 (2012) 3958–3962.
- [17] Z. Lin, G.H. Waller, Y. Liu, M. Liu, C. Wong, 3D Nitrogen-doped graphene prepared by pyrolysis of graphene oxide with polypyrrole for electrocatalysis of oxygen reduction reaction, *Nano Energy* 2 (2013) 241–248.
- [18] X. Yuan, X. Zeng, H. Zhang, Z. Ma, C. Wang, Improved performance of proton exchange membrane fuel cells with p-toluenesulfonic acid-doped co-PPy/C as cathode electrocatalyst, *J. Am. Chem. Soc.* 132 (2010) 1754–1755.
- [19] M. Xiao, J. Zhu, L. Feng, C. Liu, W. Xing, Meso/macroporous nitrogen-doped carbon architectures with iron carbide encapsulated in graphitic layers as an efficient and robust catalyst for the oxygen reduction reaction in both acidic and alkaline solutions, *Adv. Mater.* 27 (2015) 2521–2527.
- [20] D.Y. Chung, K.J. Lee, S.-H. Yu, M. Kim, S.Y. Lee, O.-H. Kim, H.-J. Park, Y.-E. Sung, Alveoli-inspired facile transport structure of N-doped porous carbon for electrochemical energy applications, *Adv. Energy Mater.* 5 (2015) 1401309.
- [21] S. Maldonado, S. Morin, K.J. Stevenson, Structure, composition, and chemical reactivity of carbon nanotubes by selective nitrogen doping, *Carbon* 44 (2006) 1429–1437.
- [22] J.P. Paraknowitsch, A. Thomas, Doping carbons beyond nitrogen: an overview of advanced heteroatom doped carbons with boron, sulphur and phosphorus for energy applications, *Energy Environ. Sci.* 6 (2013) 2839–2855.
- [23] G. Tao, L. Zhang, L. Chen, X. Cui, Z. Hua, M. Wang, J. Wang, Y. Chen, J. Shi, N-doped hierarchically macro/mesoporous carbon with excellent electrocatalytic activity and durability for oxygen reduction reaction, *Carbon* 86 (2015) 108–117.
- [24] N.P. Subramanian, X. Li, V. Nallathambi, S.P. Kumaraguru, H. Colon-Mercado, G. Wu, J.W. Lee, B.N. Popov, Nitrogen-modified carbon-based catalysts for oxygen reduction reaction in polymer electrolyte membrane fuel cells, *J. Power Sources* 188 (2009) 38–44.
- [25] J.Y. Cheon, T. Kim, Y. Choi, H.Y. Jeong, M.G. Kim, Y.J. Sa, J. Kim, Z. Lee, T.-H. Yang, K. Kwon, O. Terasaki, G.-G. Park, R.R. Adzic, S.H. Joo, Ordered mesoporous porphyrinic carbons with very high electrocatalytic activity for the oxygen reduction reaction, *Sci. Rep.* 3 (2013) 2715.
- [26] Y. Jiang, Y. Lu, X. Lv, D. Han, Q. Zhang, L. Niu, W. Chen, Enhanced catalytic performance of Pt-free iron phthalocyanine by graphene support for efficient oxygen reduction reaction, *ACS Catal.* 3 (2013) 1263–1271.
- [27] R. Jasinski, A new fuel cell cathode catalyst, *Nature* 201 (1964) 1212–1213.
- [28] S. Brüller, H. Liang, U.I. Kramm, J.W. Krumpfer, X. Feng, K. Müllen, Bimetallic porous porphyrin polymer-derived non-precious metal electrocatalysts for oxygen reduction reactions, *J. Mater. Chem. A* 3 (2015) 23799–23808.
- [29] R. Bashyam, P. Zelenay, A class of non-precious metal composite catalysts for fuel cells, *Nature* 443 (2006) 63–66.
- [30] R. Jasinski, Cobalt phthalocyanine as a fuel cell cathode, *J. Electrochem. Soc.* 112 (1965) 526–528.
- [31] Z. Chen, D. Higgins, A. Yu, L. Zhang, J. Zhang, A review on non-precious metal electrocatalysts for PEM fuel cells, *Energy Environ. Sci.* 4 (2011) 3167.
- [32] G. Nam, J. Park, S.T. Kim, D. Shin, N. Park, Y. Kim, J.-S. Lee, J. Cho, Metal-free Ketjenblack incorporated nitrogen-doped carbon sheets derived from gelatin as oxygen reduction catalysts, *Nano Lett.* 14 (2014) 1870–1876.
- [33] P. Chen, L.-K. Wang, G. Wang, M.-R. Gao, J. Ge, W.-J. Yuan, Y.-H. Shen, A.-J. Xie, S.-H. Yu, Nitrogen-doped nanoporous carbon nanosheets derived from plant biomass: an efficient catalyst for oxygen reduction reaction, *Energy Environ. Sci.* 7 (2014) 4095–4103.
- [34] K.N. Chaudhari, M.Y. Song, J.-S. Yu, Transforming hair into heteroatom-doped carbon with high surface area, *Small* 10 (2014) 2625–2636.
- [35] S. Gao, K. Geng, H. Liu, X. Wei, M. Zhang, P. Wang, J. Wang, Transforming organic-rich amaranthus waste into nitrogen-doped carbon with superior performance of the oxygen reduction reaction, *Energy Environ. Sci.* 8 (2015) 221–229.
- [36] C.-Z. Guo, W.-L. Liao, C.-G. Chen, Design of a non-precious metal electrocatalyst for alkaline electrolyte oxygen reduction by using soybean biomass as the nitrogen source of electrocatalytically active center structures, *J. Power Sources* 269 (2014) 841–847.
- [37] T. Wang, L. Wang, D. Wu, W. Xia, H. Zhao, D. Jia, Hydrothermal synthesis of nitrogen-doped graphene hydrogels using amino acids with different acidities as doping agents, *J. Mater. Chem. A* 2 (2014) 8352–8361.
- [38] J. Maruyama, N. Fukui, M. Kawaguchi, I. Abe, Application of nitrogen-rich amino acids to active site generation in oxygen reduction catalyst, *J. Power Sources* 182 (2008) 489–495.
- [39] C.H. Choi, S.H. Park, S.I. Woo, Heteroatom doped carbons prepared by the pyrolysis of bio-derived amino acids as highly active catalysts for oxygen electro-reduction reactions, *Green Chem.* 13 (2011) 406–412.
- [40] J. Yan, H. Meng, F. Xie, X. Yuan, W. Yu, W. Lin, W. Ouyang, D. Yuan, Metal free nitrogen doped hollow mesoporous graphene-analogous spheres as effective electrocatalyst for oxygen reduction reaction, *J. Power Sources* 245 (2014) 772–778.

- [41] J. Kang, H. Wang, S. Ji, J. Key, R. Wang, Synergy among manganese, nitrogen and carbon to improve the catalytic activity for oxygen reduction reaction, *J. Power Sources* 251 (2014) 363–369.
- [42] R. Gokhale, S.M. Unni, D. Puthusseri, S. Kurungot, S. Ogale, Synthesis of an efficient heteroatom-doped carbon electro-catalyst for oxygen reduction reaction by pyrolysis of protein-rich pulse flour cooked with SiO<sub>2</sub> nanoparticles †, *Phys. Chem. Chem. Phys.* 16 (2014) 4251–4259.
- [43] S. Lee, D.-H. Kwak, S.-B. Han, E.-T. Hwang, M.-C. Kim, J.-Y. Lee, Y.-W. Lee, K.-W. Park, Synthesis of hollow carbon nanostructures as a non-precious catalyst for oxygen reduction reaction, *Electrochim. Acta* 191 (2016) 805–812.
- [44] S. Lee, D.-H. Kwak, S.-B. Han, Y.-W. Lee, I.-A. Choi, H.-S. Park, J.-Y. Park, K.-W. Park, Bimodal porous iron/nitrogen-doped highly crystalline carbon nanostructure as a cathode catalyst for oxygen reduction reaction in an acid medium, *ACS Catal.* 6 (2016) 5095–5102.
- [45] Y. Baskin, L. Meyer, Lattice constants of graphite at low temperatures, *Phys. Rev.* 100 (1955) 544.
- [46] M.J. Mcallister, J.-L. Li, D.H. Adamson, H.C. Schniepp, A.A. Abdala, J. Liu, M. Herrera-Alonso, D.L. Milius, R. Car, R.K. Prud'homme, I.A. Aksay, Single sheet functionalized graphene by oxidation and thermal expansion of graphite, *Chem. Mater.* 19 (2007) 4396–4404.
- [47] S. Tomita, A. Burian, J.C. Dore, D. LeBolloch, M. Fujii, S. Hayashi, Diamond nanoparticles to carbon onions transformation: X-ray diffraction studies, *Carbon* 40 (2002) 1469–1474.
- [48] X.B. Wu, P. Chen, J. Lin, K.L. Tan, Hydrogen uptake by carbon nanotubes, *Int. J. Hydrogen Energy* 25 (2000) 261–265.
- [49] Z. Schniepp, Y. Zhang, M.J. Hollamby, B.R. Pauw, M. Tanaka, Y. Matsushita, Y. Sakka, Doped-carbon electrocatalysts with trimodal porosity from a homogeneous polypeptide gel, *J. Mater. Chem. A* 1 (2013) 13576–13581.
- [50] C. Hu, L. Wang, Y. Zhao, M. Ye, Q. Chen, Z. Feng, L. Qu, Designing nitrogen-enriched echinus-like carbon capsules for highly efficient oxygen reduction reaction and lithium ion storage, *Nanoscale* 6 (2014) 8002–8009.
- [51] W. Yuan, Y. Zhou, Y. Li, C. Li, H. Peng, J. Zhang, Z. Liu, L. Dai, G. Shi, The edge- and basal-plane-specific electrochemistry of a single-layer graphene sheet, *Sci. Rep.* 3 (2013) 2248.
- [52] R. Silva, J. Al-Sharab, T. Asefa, Edge-plane-rich nitrogen-doped carbon nanoneedles and efficient metal-free electrocatalysts, *Angew. Chem. Int. Ed.* 51 (2012) 7171–7175.
- [53] H. Peng, F. Liu, X. Liu, S. Liao, C. You, X. Tian, H. Nan, F. Luo, H. Song, Z. Fu, P. Huang, Effect of transition metals on the structure and performance of the doped carbon catalysts derived from polyaniline and melamine for ORR application, *ACS Catal.* 4 (2014) 3797–3805.
- [54] X. Wen, D. Zhang, L. Shi, T. Yan, H. Wang, J. Zhang, Three-dimensional hierarchical porous carbon with a bimodal pore arrangement for capacitive deionization, *J. Mater. Chem.* 22 (2012) 23835–23844.
- [55] X. Wen, D. Zhang, T. Yan, J. Zhang, L. Shi, Three-dimensional graphene-based hierarchically porous carbon composites prepared by a dual-template strategy for capacitive deionization, *J. Mater. Chem. A* 1 (2013) 12334–12344.
- [56] M. Lefèvre, J.P. Dodelet, P. Bertrand, Molecular oxygen reduction in PEM fuel cells: evidence for the simultaneous presence of two active sites in Fe-based catalysts, *J. Phys. Chem. B* 106 (2002) 8705–8713.
- [57] M. Lefèvre, J.P. Dodelet, P. Bertrand, O<sub>2</sub> reduction in PEM fuel cells: activity and active site structural information for catalysts obtained by the pyrolysis at high temperature of Fe precursors, *J. Phys. Chem. B* 104 (2000) 11238–11247.
- [58] V.V. Strelko, V.S. Kuts, P.A. Thrower, On the mechanism of possible influence of heteroatoms of nitrogen, boron and phosphorus in a carbon matrix on the catalytic activity of carbons in electron transfer reactions, *Carbon* 38 (2000) 1499–1524.
- [59] C.V. Rao, C.R. Cabrera, Y. Ishikawa, In search of the active site in nitrogen-doped carbon nanotube electrodes for the oxygen reduction reaction, *J. Phys. Chem. Lett.* 1 (2010) 2622–2627.
- [60] G. Liu, X. Li, J.-W. Lee, B.N. Popov, A review of the development of nitrogen-modified carbon-based catalysts for oxygen reduction at USC, *Catal. Sci. Technol.* 1 (2011) 207.
- [61] D. Guo, R. Shibuya, C. Akiba, S. Saji, T. Kondo, J. Nakamura, Active sites of nitrogen-doped carbon materials for oxygen reduction reaction clarified using model catalysts, *Science* 351 (2016) 361–365.
- [62] H. Peng, Z. Mo, S. Liao, H. Liang, L. Yang, F. Luo, H. Song, Y. Zhong, B. Zhang, High performance Fe- and N-doped carbon catalyst with graphene structure for oxygen reduction, *Sci. Rep.* 3 (2013) 1765.
- [63] M. Li, Y. Xiong, X. Liu, C. Han, Y. Zhang, X. Bo, L. Guo, Iron and nitrogen co-doped carbon nanotube/hollow carbon fibers derived from plant biomass as efficient catalysts for the oxygen reduction reaction, *J. Mater. Chem. A* 3 (2015) 9658–9667.
- [64] J. Chen, X. Cui, W. Zheng, The role of trace Fe in Fe-N-doped amorphous carbon with excellent electrocatalytic performance for oxygen reduction reaction, *Catal. Commun.* 60 (2015) 37–41.
- [65] V. Nallathambi, J.-W. Lee, S.P. Kumaraguru, G. Wu, B.N. Popov, Development of high performance carbon composite catalyst for oxygen reduction reaction in PEM Proton Exchange Membrane fuel cells, *J. Power Sources* 183 (2008) 34–42.
- [66] Z.-Y. Yuan, B.-L. Su, Insights into hierarchically meso–macroporous structured materials, *J. Mater. Chem.* 16 (2006) 663–677.
- [67] B. Fang, J.H. Kim, M.-S. Kim, J.-S. Yu, Hierarchical nanostructured carbons with meso–macroporosity: design, characterization, and applications, *Acc. Chem. Res.* 46 (2013) 1397–1406.
- [68] L.-F. Chen, X.-D. Zhang, H.-W. Liang, M. Kong, Q.-F. Guan, P. Chen, Z.-Y. Wu, S.-H. Yu, Synthesis of nitrogen-doped porous carbon nanofibers as an efficient electrode material for supercapacitors, *ACS Nano* 6 (2012) 7092–7102.
- [69] Z.-S. Wu, Y. Sun, Y.-Z. Tan, S. Yang, X. Feng, K. Müllen, Three-dimensional graphene-based macro- and mesoporous frameworks for high-performance electrochemical capacitive energy storage, *J. Am. Chem. Soc.* 134 (2012) 19532–19535.
- [70] N. Ramaswamy, S. Mukerjee, Fundamental mechanistic understanding of electrocatalysis of oxygen reduction on Pt and non-Pt surfaces: acid versus alkaline media, *Adv. Phys. Chem.* 2012 (2012) 491604.
- [71] M.S. Thorum, J.M. Hankett, A.A. Gewirth, Poisoning the oxygen reduction reaction on carbon-supported Fe and Cu electrocatalysts: evidence for metal-centered activity, *J. Phys. Chem. Lett.* 2 (2011) 295–298.
- [72] W. Li, A. Yu, D.C. Higgins, B.G. Llanos, Z. Chen, Biologically inspired highly durable iron phthalocyanine catalysts for oxygen reduction reaction in polymer electrolyte membrane fuel cells, *J. Am. Chem. Soc.* 132 (2010) 17056–17058.
- [73] S. Gupta, C. Fierro, E. Yeager, The effects of cyanide on the electrochemical properties of transition metal macrocycles for oxygen reduction in alkaline solutions, *J. Electroanal. Chem.* 306 (1991) 239–250.
- [74] H.-W. Liang, Z.-Y. Wu, L.-F. Chen, C. Li, S.-H. Yu, Bacterial cellulose derived nitrogen-doped carbon nanofiber aerogel: an efficient metal-free oxygen reduction electrocatalyst for zinc-air battery, *Nano Energy* 11 (2015) 366–376.
- [75] H. Peng, Z. Mo, S. Liao, H. Liang, L. Yang, F. Luo, H. Song, Y. Zhong, B. Zhang, High performance Fe- and N-doped carbon catalyst with graphene structure for oxygen reduction, *Sci. Rep.* 3 (2013) 1765.
- [76] F. Liu, H. Peng, C. You, Z. Fu, P. Huang, H. Song, S. Liao, High-performance doped carbon catalyst derived from nori biomass with melamine promoter, *Electrochim. Acta* 138 (2014) 353–359.
- [77] Y. Li, H. Zhang, P. Liu, Y. Wang, H. Yang, Y. Li, H. Zhao, Self-supported bimodal-pore structured nitrogen-doped carbon fiber aerogel as electrocatalyst for oxygen reduction reaction, *Electrochem. Commun.* 51 (2015) 6–10.